



Cite this: *Soft Matter*, 2024, 20, 4998

There and back again: bridging meso- and nano-scales to understand lipid vesicle patterning[†]

Julie Cornet,^a Nelly Coulonges,^{ab} Weria Pezeshkian,^{ID}^c Maël Penissat-Mahaut,^b Hermes Desgrez-Dautet,^d Siewert J. Marrink,^{ID}^e Nicolas Destainville,^{*,a} Matthieu Chavent^{ID}^{*,bd} and Manoel Manghi^{ID}^{*,a}

We describe a complete methodology to bridge the scales between nanoscale molecular dynamics and (micrometer) mesoscale Monte Carlo simulations in lipid membranes and vesicles undergoing phase separation, in which curving molecular species are furthermore embedded. To go from the molecular to the mesoscale, we notably appeal to physical renormalization arguments enabling us to rigorously infer the mesoscale interaction parameters from its molecular counterpart. We also explain how to deal with the physical timescales at stake at the mesoscale. Simulating the as-obtained mesoscale system enables us to equilibrate the long wavelengths of the vesicles of interest, up to the vesicle size. Conversely, we then backmap from the meso- to the nano-scale, which enables us to equilibrate in turn the short wavelengths down to the molecular length-scales. By applying our approach to the specific situation of patterning a vesicle membrane, we show that macroscopic membranes can thus be equilibrated at all length-scales in achievable computational time offering an original strategy to address the fundamental challenge of timescale in simulations of large bio-membrane systems.

Received 20th January 2024,
Accepted 12th May 2024

DOI: 10.1039/d4sm00089g

rsc.li/soft-matter-journal

1 Introduction

The physics of living systems is permanently confronted by the multiplicity of the length- and time-scales of interest: from the nanoscopic molecular scale where events occur below the nano-second timescale, to the micrometric cellular scale where microseconds or seconds are at stake. Different physical and numerical techniques have been developed to study these different scales, which are either quantum or classical, with explicit or implicit water, including stochastic or hydrodynamics techniques. But bridging these scales is still a difficult task as the methods employed for each scale may not use the same physical dynamics – *e.g.*, molecular dynamics (MD) or Monte Carlo (MC) – nor the same integration scheme – *e.g.*, Newtonian or Brownian dynamics. Thus, even though multi-scale workflows have been

developed recently,^{1–3} these types of approaches have been limited in terms of the spatial/timing range they can span⁴ and they have generally been constrained to “one spatial direction”,^{5–8} from the nanoscale to the meso/micro-scale or the other way around. Here, thanks to recent advances in the field,^{9,10} we provide details of and rationalize a method to fully bridge, forward and backward, nano- and meso-scales in biomembranes (see Fig. 1).

We developed this approach in the specific context of lipidic biomembrane patterning. With the recent *in vivo*, *in vitro*, and *in silico* developments, it is now recognized that cell membrane components are not homogeneously distributed, but are organized into functional lipid and protein sub-micrometric domains.^{12–18} These nanodomains play fundamental roles in cell biology, especially as they serve as platforms or micro-reactors for many biological functions such as infections (viral or bacterial), cell adhesion, transport of solutes, or signaling. Thus, deciphering the formation and evolution of these domains is essential to fully understand these fundamental biological processes. Among the mechanisms proposed for their formation, the role of spontaneous curvature induced by different membrane constituents, with specific shapes, is the focus of particular attention.¹⁹

For example, the glycosphingolipid GM1 has a bulky head comprised of four monosaccharides resulting in this lipid having an overall conical shape^{17,20} (see Fig. 1a). Present predominantly in the outer cell membrane,^{21,22} this lipid can act as a membrane anchor for different toxins, bacteria and

^a Laboratoire de Physique Théorique, Université de Toulouse, CNRS, UPS, France.

E-mail: nicolas.destainville@univ-tlse3.fr, manoel.manghi@univ-tlse3.fr

^b Institut de Pharmacologie et Biologie Structurale, Université de Toulouse, CNRS, Université Toulouse III - Paul Sabatier, 31400, Toulouse, France.

E-mail: matthieu.chavent@univ-tlse3.fr

^c Niels Bohr International Academy, Niels Bohr Institute, University of Copenhagen, Blegdamsvej 17, 2100 Copenhagen, Denmark

^d Laboratoire de Microbiologie et Génétique Moléculaires (LMGM), Centre de Biologie Intégrative (CBI), Université de Toulouse, CNRS, UPS, France

^e Groningen Biomolecular Sciences and Biotechnology Institute, University of Groningen, Nijenborgh 7, 9747 AG Groningen, The Netherlands

[†] Electronic supplementary information (ESI) available: Supplementary text and 6 figures. See DOI: <https://doi.org/10.1039/d4sm00089g>



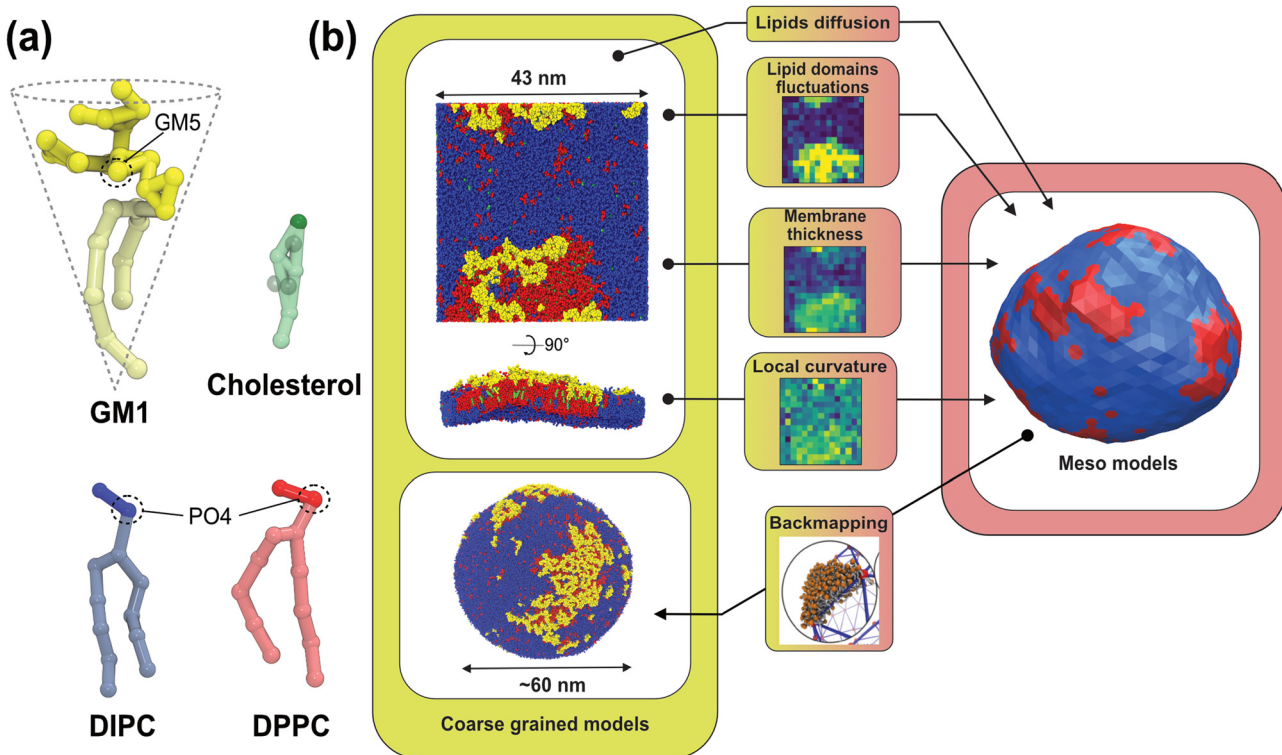


Fig. 1 Principle of our multiscale modeling scheme for lipid membranes. (a) The lipid models used in the CG simulations. The GM1 model corresponds to the monosialotetrahexosylganglioside and cholesterol model,¹¹ the DIPC model corresponds to 1,2-dilinoleoyl-*sn*-glycero-3-phosphocholine, and the DPPC model corresponds to 1,2-dipalmitoyl-*sn*-glycero-3-phosphocholine. The most hydrophilic parts of the lipids are represented in darker colors while the lighter colors depict the more hydrophobic parts of the models. The PO4 and GM5 beads used to define the membrane surface are outlined on the different lipids (see the methods section). (b) From the CG molecular dynamics simulations (upper-left panel), we infer the physical parameters required by the mesoscale Monte Carlo model (right panel) consisting of a bi-phasic tessellated vesicle. The extraction of these parameters is illustrated in the central panels. They are: (i) two dynamical parameters relating the time-scales of lipid diffusion in the membrane plane, and transverse membrane fluctuations; (ii) lipid domain boundary fluctuations from which is inferred the line tension between both lipid phases; (iii) the membrane thickness difference between phases, from which bending moduli ratio can be inferred, and (iv) the spontaneous curvature of the Lo phase induced by insertion of GM1 in the upper leaflet. Conversely, the Meso-to-CG backmapping at the full vesicle scale (lower-left) is illustrated in the lower-middle panel.

viruses^{23,24} and plays important roles in several neuronal processes and diseases, notably auto-immune ones.^{24,25} Although knowledge about its lateral organization remains an active field of research,²² the properties of GM1 are thought to be linked to its propensity to curve the membrane, ensuing from its conical shape.^{21,26,27} To test this hypothesis on well-defined model systems, giant unilamellar vesicles (GUVs) were used to better characterize *in vitro* the relationship between curvature generation and lipid domain formation.^{21,27–29} However, fully linking microscopy visualization, with an intrinsically limited resolution, to nanoscale partitioning of the lipids, is still a challenge.

On the one hand, MD simulations are suitable tools to understand how GM1 perturbs the lipid membrane organization at the molecular scale, notably by curving the bilayer,³⁰ or by destabilizing lipid–lipid phase separation in multicomponent membranes.²² On the other hand, describing the effect of phase separation combined with intrinsic curvature at vesicular or cellular scales makes the use of a much larger degree of coarse-graining inevitable. Here, we illustrate how to bridge the theoretical gap between Coarse-Grained Molecular Dynamics

(CG-MD) simulations and mesoscale (Meso for short) Monte Carlo simulations^{31,32} focusing on vesicular systems, as shown in Fig. 1. Using physically relevant concepts, we first show which data to extract at the nanoscale, obtained with CG-MD simulations, and how they can be used to parametrize the mesoscale Monte Carlo model. We then go from the nano- to meso-scale by integrating out microscopic degrees of freedom, a non-trivial task due to renormalization issues,³³ that we fully take into account in this work. Then we show how this leads to meaningful results for the mesoscale model, allowing one to equilibrate membrane patterning at the scale of a whole vesicle, and how this model can predict experimental data at micrometric scales. Finally, we explain how to scale back to CG models to equilibrate the short length-scales, and decipher the overall organization of large lipid domains down to the nanoscale. We also discuss the feasibility of our approach and the limitations inherent to each model when one passes from one scale to another. This thorough approach to linking the scales combined with careful explanations of how to extract meaningful data will pave the way for further development of fully integrated multiscale workflows.

2 Methods

2.1 Coarse-grained (MARTINI) molecular dynamics simulations

We use the CHARMM-GUI *MARTINI Maker*^{34,35} to generate $43 \times 43 \text{ nm}^2$ lipid bilayer systems. The membrane patches are surrounded by about 4 nm of water on each side. Ions are added to neutralize the system. We study a mixture of C16:0 dipalmitoyl PC (DPPC), C18:2 dilinoleoyl PC (DLiPC), also named DIPC in the MARTINI force field, and cholesterol with a concentration ratio of 30:58:12 and with varying concentrations of C(d18:1/18:0) *N*-stearoyl-*d*-erythro (GM1) in the upper leaflet (given in mol mol⁻¹) (see Table 1).

The CG-MD simulations are performed using the MARTINI v2.2³⁶ force field in the NPT ensemble and run with GROMACS 2016 software.³⁷ The temperature is set to 310 K at which Lo and Ld phases coexist for these lipid mixtures. We use the velocity rescaling thermostat³⁸ coupled to a semi-isotropic Parrinello-Rahman barostat³⁹ with a pressure of 1 bar. The standard time step of 20 fs is used for all simulations. All systems are equilibrated following equilibration steps as described in the Membrane Builder workflow.⁴⁰ For production, all the planar systems are simulated for 20 μs to ensure convergence.

The analysis scripts are written in Python3 using MDAnalysis packages.⁴¹ In particular, we use the LeafletFinder tool that allows identifying upper and lower leaflets.

2.2 Mesoscale model

The mesoscale model used in the present work was developed and validated previously by one of our groups. We provide an overview of the model in this section, and the interested reader can refer to previously published work for further details.^{42,43}

2.2.1 Discretization of the membrane model. We discretize space, time, and accordingly, the calculation of the system free energy. We consider the initial vesicle as a tessellated sphere composed of N vertices.⁴² An initial icosahedron is tessellated iteratively. This leads to accessible values for the total number of vertices $N = 10 \times 4^k + 2$.⁴⁴ Each vertex represents a small patch of one of the two species (delineated to the Voronoï cell associated with the vertex). The real size of this patch depends on the average vesicle radius R . In the case of weak shape deformations, the area A_0 of a patch is approximately $A_0 \simeq 4\pi R^2/N$. For example, for $N = 2562$ sites ($k = 4$ iterations), in a small vesicle of radius $R = 100 \text{ nm}$, a patch would contain about

Table 1 Summary of the CG systems simulated (see also Fig. 3). The vesicle has the composition (DPPC–DIPC–Chol + 15% GM1). Durations are in μs

System	Particles	Duration
DPPC–DIPC–Chol	167 409	20
DPPC–DIPC–Chol + 2.5% GM1	279 234	20
DPPC–DIPC–Chol + 5% GM1	181 285	20
DPPC–DIPC–Chol + 7.5% GM1	279 981	20
DPPC–DIPC–Chol + 10% GM1	181 756	20
DPPC–DIPC–Chol + 15% GM1	207 647	20
Vesicle	3 487 094	10

100 lipids. Two neighboring vertices are separated by the average lattice spacing

$$a = \left(\frac{8\pi}{\sqrt{3}}\right)^{\frac{1}{2}} \frac{R}{\sqrt{N}}. \quad (1)$$

2.2.2 Helfrich free energy. In the continuous case, the Helfrich elastic free energy is

$$H_{\text{Helf}} = \frac{1}{2} \int \kappa (2H - C)^2 dS + \sigma \mathcal{A} \quad (2)$$

where κ is the (local) bending elastic modulus, σ is the surface tension and \mathcal{A} is the total vesicle area. $2H$ is the total curvature, *i.e.* the sum of the two principal curvatures, and C is the (local) spontaneous curvature imposed by the molecular species. We do not account for the Gaussian curvature in this model. Using the Laplace–Beltrami operator⁴⁵ for the curvature term, the discrete elastic free energy reads

$$H_{\text{Helf}} = \frac{1}{2} \sum_i \kappa_i [2H_i - C_i]^2 \mathcal{A}_i + \sigma \sum_i \mathcal{A}_i \quad (3)$$

where \mathcal{A}_i is the area associated with a vertex ($\mathcal{A}_i = A_0$ at the start). The total curvature $2H_i$ is obtained as the signed norm of the Laplace–Beltrami operator \mathbf{K}_i

$$\mathbf{K}_i = \frac{1}{2\mathcal{A}_i} \sum_j (\cot \alpha_{ij} + \cot \beta_{ij})(\mathbf{r}_i - \mathbf{r}_j) \quad (4)$$

Here \mathbf{r}_i is the position of vertex i and the sum is taken over its first neighbors j and the angles α_{ij} and β_{ij} are the angles of the two triangles sharing the edge $(\mathbf{r}_i, \mathbf{r}_j)$ and opposite to this edge.^{42,43} Both κ_i and C_i might be vertex-dependent in the case of bi- or multi-phasic systems, see below. We use the reduced membrane tension $\tilde{\sigma} = \sigma R^2/(k_B T)$.

The vesicle volume V is fixed close to the initial volume V_0 by a hard quadratic constraint. Hence the following energy term is added to the Helfrich energy

$$H_V = \frac{1}{2} K_V \left(\frac{V}{V_0} - 1 \right)^2 \quad (5)$$

where $K_V = 2 \times 10^6 k_B T$. In contrast, the total vesicle area is constrained by a soft constraint and controlled by the surface tension σ .

2.2.3 Species characteristics and interactions. We use the discrete two-dimensional Ising (or lattice-gas) model to describe the Lo/Ld binary mixture.⁴⁶ The fact that membrane lipid binary mixtures belong to the 2D Ising universality class has been experimentally checked in ref. 13. The Ising model Hamiltonian reads

$$H_I = -J_I \sum_{\langle i,j \rangle} s_i s_j \quad (6)$$

where $s_i = \pm 1$ and the sum is done on nearest-neighbor vertex pairs. The tessellation of the sphere that we use is a triangular lattice, with each vertex having 6 neighbors, except for the 12 vertices originating from the original icosahedron, which have

only 5 neighbors. The lattice-gas composition, $\phi_i = 0$ or 1 , on any vertex i of the tessellated lattice is related to its “spin” s_i through $\phi_i = (1 + s_i)/2$. The Ising constant $J_I > 0$ measures the strength of short-range affinities between membrane constituents. In our case, we work at a fixed $\sum_i s_i$ and thus at a fixed concentration $\phi = \sum_i \phi_i/N$ and temperature T . Varying the temperature between the different simulations of the Ising model amounts to varying the Ising coupling J_I . In our simulations we chose to fix the temperature T and to tune the value of J_I . Its exact critical value where the phase transition takes place is $J_{I,c} = (\ln 3/4)k_B T \simeq k_B T/3.64$ on an infinite triangular lattice,⁴⁷ which means that if $J_I < J_{I,c}$ (resp. $J_I > J_{I,c}$), then the system is in the disordered (resp. ordered) phase.

The local spontaneous curvature $C_i = C(\phi_i)$ used in eqn (3) depends on the local concentration ϕ_i and can take two values in the mesoscopic model, $C_0 = 2/R$ for the Ld phase and $C_{\text{Lo+GM1}}^{\text{vesicle}}$ for the Lo + GM1 one (see below). Similarly, the local bending modulus $\kappa_i = \kappa(\phi_i)$ can take two values, κ_{Ld} and κ_{Lo} . In this work, for simplicity, κ_{Lo} does not depend on the GM1 concentration in the simulations.

We used the mesoscale code developed in ref. 42 and 43 to simulate fluctuating vesicles. At each Monte Carlo step, two local movement attempts are applied to randomly chosen vertices: (1) a single vertex undergoes a small radial displacement δr according to the Metropolis rule, which locally modifies the elastic energy; (2) the compositions ϕ_i of two neighboring vertices are swapped, modifying the interaction energy as well as the elastic energy through the elastic parameters $\kappa(\phi_i)$ and $C(\phi_i)$ above. Since we consider a system with a conserved order parameter ϕ , we use the Kawasaki algorithm.⁴⁸

Contrary to alternative models in the spirit of the Dynamic Triangulated Surface (DTS) one,^{1,33,49–52} edge flips are not allowed in the tessellated system and vertex moves are only radial, and consequently no constraint on edge lengths needs to be applied in the present model. In compensation, our model is valid in the vesicle quasi-spherical regime only. For more information refer to ref. 43 in which the whole simulation scheme is described and discussed in detail.

2.3 Extraction of line tension from domain boundary fluctuations

As shown in Fig. 2, we use a new discretization of the plane, in the form of a “dartboard” made of n_c concentric circles, centered on the domain geometric barycenter and separated by $\delta r = 2$ nm, as well as $n_a = 20$ angular sectors. In each box of the as-obtained “dartboard”, we use the same majority rule as in the square mesh (see Section 3.1.2 below) so as to identify the boxes belonging to the Lo domain and those belonging to the Ld surrounding phase. Starting from the center and following the rays, we then identify the boundary where at least two successive Ld boxes (or the last circle) are encountered, so that small bubbles of the Ld phase are not considered as being part of the boundary. This defines a discrete version of the domain boundary $r(\theta)$.

We then use eqn (3) from ref. 53 to directly link the power spectrum of the boundary fluctuations to the line tension λ of

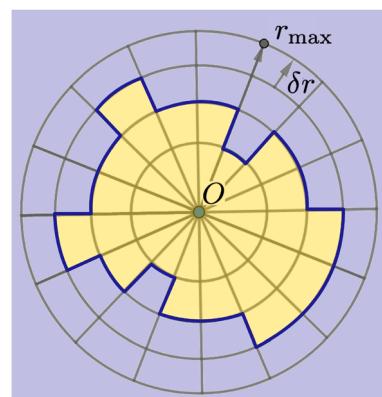


Fig. 2 Principle of the polar discretization of the Lo domain in order to locate its boundary (dark blue line) with a (discrete) polar function $r(\theta)$. The “dartboard” is divided into $n_c = r_{\text{max}}/\delta r$ concentric circles and n_a regularly spaced angular sectors, thus defining $n_c \times n_a$ boxes in which the majority rule is applied to determine whether they belong to the Lo (yellow) or the Ld (light blue) phase.

the mixture. However, we use a different convention for the Fourier coefficients:

$$u_n = \frac{1}{2\pi} \int_0^{2\pi} u(\theta) e^{-ni\theta} d\theta \quad (7)$$

that we estimate by discretizing the integral. Here $u(\theta)$ is defined by $r(\theta) = R_0[1 + u(\theta)]$. It can then be shown that

$$\langle |u_n|^2 \rangle = \frac{k_B T}{2\lambda\pi R_0(n^2 - 1)} \quad (8)$$

in equilibrium, for $n > 1$. The mode $n = 1$ corresponds to a translation of the whole domain and its value is non-physical as it simply reflects the error possibly made when identifying the domain barycenter. In this equation R_0 is the equivalent radius of a non-fluctuating domain of area πR_0^2 . In principle, it is different from the average domain radius $\langle r(\theta) \rangle = R_0 \left(1 - \sum_{n>0} \langle |u_n|^2 \rangle \right) < R_0$.⁵³ In practice, however, R_0 is close to $\langle r(\theta) \rangle$ for the line tension values at play here and we identify both.

2.4 Relationship between the CG extracted parameters and the mesoscale model ones

In order to bridge the two modeling scales, the coarse-grained and mesoscale ones, we need to establish the link between the parameters that we measure in the CG-MD simulations with the input parameters of the mesoscale description. This can lead to technical difficulties, as outlined below.

Due to renormalization issues,⁵³ the Ising parameter depends on the coarse-graining level because it must account for the microscopic degrees of freedom integrated out in the coarse-graining process. We denote by

- a the simulation lattice spacing at the mesoscale, *i.e.* the average length-size of the elementary tessellation triangles, see eqn (1).

- $l_0 \sim 1$ nm the typical distance between lipids at the molecular scale,



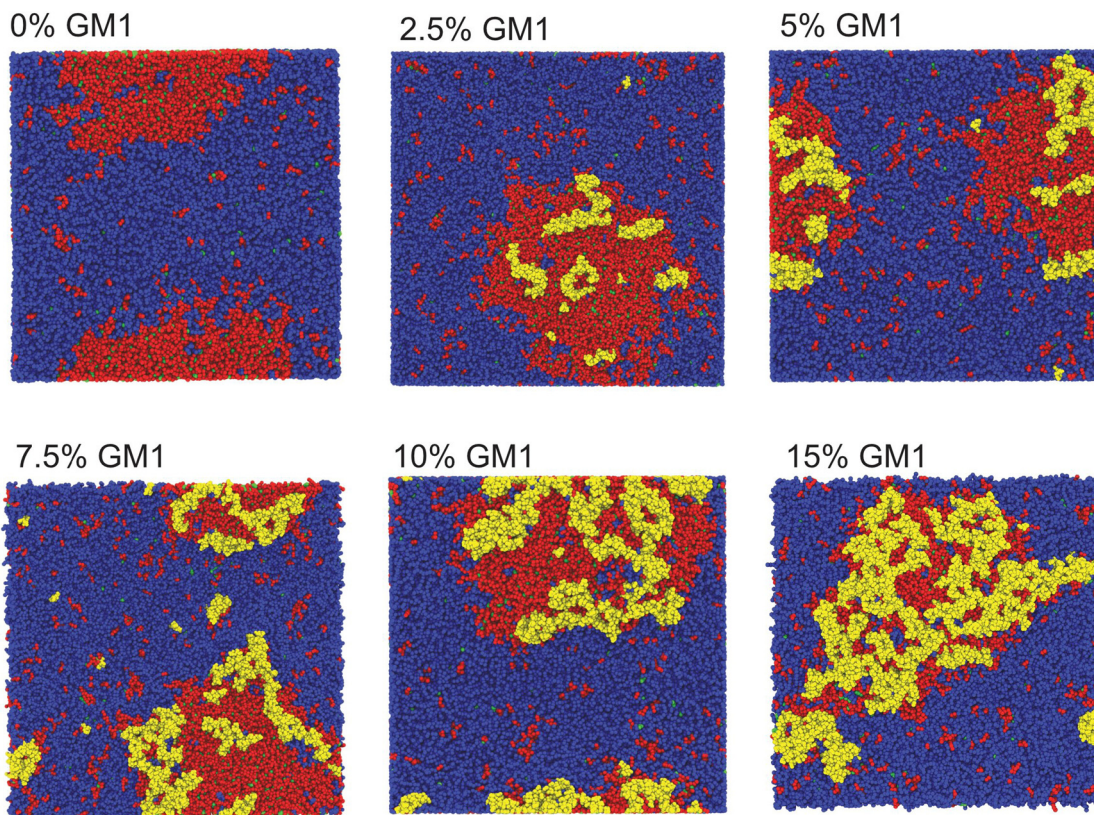


Fig. 3 Top view of CG-MD membrane systems with different molar concentrations of GM1 at 20 μ s. The membrane phase separates in all the systems forming a Lo domain enriched in DPPC, GM1, and cholesterol surrounded by a Ld domain enriched in DIPC. Due to the boundary conditions, the Lo domain is sometimes visually divided into two parts but it is a visualization artefact. GM1 lipids are depicted in yellow, DPPC in red, DIPC in blue, and cholesterol in green.

• $J_{I,0}$ the Ising interaction parameter at the molecular scale, of critical value $J_{I,c}$. It is directly related to the Flory parameter χ of the binary mixture.⁵⁴

We assume that the interaction network at the molecular scale can be assimilated to a triangular lattice, due to the symmetries of bidimensional liquids. Close to the critical point, one has

$$J_I - J_{I,c} = \frac{a}{l_0} (J_{I,0} - J_{I,c}) \quad (9)$$

thus relating the two scales.³³ For this lattice $k_B(T_c - T) = (4/\ln 3)(J_{I,0} - J_{I,c})$ close to T_c , where T_c can be measured either in experiments or in molecular dynamics simulations. After measuring the line tension λ as explained in the text, we can have access to the Ising parameter at the molecular scale. Indeed, close to the critical point, λ depends algebraically on $J_{I,0} - J_{I,c}$ and vanishes at the critical point. Renormalization arguments also show that both quantities are in fact proportional for the 2D Ising model universality class. More precisely,

$$\lambda = \frac{4\sqrt{3}}{l_0} (J_{I,0} - J_{I,c}). \quad (10)$$

close to $J_{I,c}$. The prefactor depends on the lattice and is equal to

$4\sqrt{3}$ on a triangular lattice.⁵⁵ Due to eqn (9), we thus also have

$$\lambda = \frac{4\sqrt{3}}{a} (J_I - J_{I,c}). \quad (11)$$

This will enable us below to calculate the Ising parameter J_I of the mesoscale simulations through the measurement of the line tension λ in the CG simulations. Note that this relationship (11) holds independently of the value of the Ising parameter $J_{I,0}$ at the molecular scale that we will not need to be evaluated. Its value can be inferred from the measurement of λ and eqn (10) if needed.

The analysis of bilayer simulations at the molecular level thus provides realistic membrane parameter values that can be injected into the mesoscale model. In this way, the simulations can then be tuned in order to tackle different biologically relevant systems at large length and time scales. Note that the bending moduli κ depend only logarithmically on the scale a ,⁵⁶ and we thus consider them as a constant for the sake of simplicity.

2.5 Backmapping from the mesoscale to the coarse-grained scale

The mesoscale model can be backmapped to CG resolution (Martini 2.2) based on the TS2CG approach of ref. 9. We follow



Table 2 Input parameters used by TS2CG (see also Fig. 3). APL means Area Per Lipid, in nm²

Lipid type	Upper leaflet	Lower leaflet	APL
Ld domain			
DPPC	0.06	0.06	0.68
DIPC	0.91	0.91	0.77
CHOL	0.03	0.03	0.5
Lo domain			
DPPC	0.40	0.68	0.68
DIPC	0.04	0.04	0.77
CHOL	0.28	0.28	0.5
GM1	0.28	0	0.7

the different steps presented in the TS2CG tutorial (<https://cgmartini.nl/index.php/2021-martini-online-workshop/tutorials/558-9-ts2cg>). Briefly, the last frame from the mesoscale model is saved in a dynamic triangulated surface (DTS) file format readable by the TS2CG program. In this file, both Lo and Ld domains were defined as well as the overall shape of the vesicle using labeled triangles. TS2CG inputs such as lipid concentrations and Area Per Lipid (APL) are extracted from the previous CG simulation of a planar system with 15% of GM1. These values are presented in Table 2.

We perform 1000 steps of standard energy minimization and 5000 steps of molecular dynamics runs with lipid head-group positions restrained to relax the lipid chains. We perform these steps without solvent particles using the Dry Martini force field.⁵⁷ Next, the vesicle membrane is solvated by propagating an equilibrated Martini water box in the system and removing any water particle within a certain cutoff from the membrane particles as done previously.⁵⁸

The solvated system is then equilibrated following several steps of equilibration as carried out for the planar systems (see above). For these steps, the constraints beads, called Wall, are present to keep the overall shape of the vesicle (see ref. 9 for more details). Then, we remove the wall beads and performed 10 μs of production using the same thermostat and barostat parameters as for the planar systems (see above) with isotropic pressure coupling.

In equilibrated vesicles, the two leaflets do not have the same area for geometrical reasons and thus have different molecule numbers. In experiments on vesicles, equilibration is a rather slow process ensured by thermally activated lipid flip-flops. Such flip-flops cannot occur at the rapid simulation timescale, so that one must take care of filling in each leaflet with the appropriate molecule number. This is guaranteed by TS2CG.

3 Results

3.1 Nanoscale analysis of lipid phase separation and GM1 partitioning

We have performed CG-MD simulations of 43 × 43 nm² bilayers made of a DPPC-DIPC-Chol mixture with varying molar concentrations of GM1 molecules in the upper leaflet from 0% up to 15% (see the methods section). The duration of these simulations is set to 20 μs. The DPPC-DIPC-Chol mixture allows these systems to undergo phase separation where a phase enriched in

DPPC and cholesterol molecules called the liquid-ordered (Lo) phase and another phase enriched in DIPC, the liquid-disordered phase (Ld) coexist,^{22,59–61} as displayed in Fig. 3.

3.1.1 Convergence to equilibrium depends on GM1 concentration.

In order to quantify the phase separation degree and its evolution with time, we compute the mean number of neighbors of the same species for each lipid throughout the simulation and plot it over time. Indeed, in a binary mixture controlled by short range interactions, the average energy per molecule is directly directed to the average composition of its immediate neighborhood. We use a cut-off distance $d = 13 \text{ \AA}$ to define the neighborhood zone, in order to have about six neighbors per molecule in equilibrium, as in a simple two-dimensional liquid. Without GM1, this observable reaches a plateau shortly after 5 μs (Fig. 4a). Its value is lower than the average number of neighbors since a finite fraction of molecules have some neighbors of a different species. To compare systems with different concentrations of GM1, we fit this curve with a single exponential $\langle n(t) \rangle = A - Be^{-t/\tau}$ as shown in Fig. 4b. We measure relaxation times τ on the order of a few μs. This

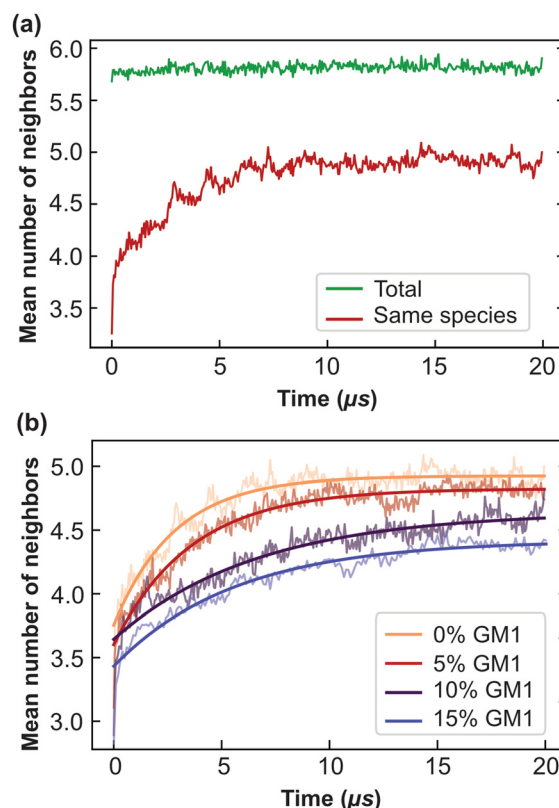


Fig. 4 The mean number of neighbors and convergence to equilibrium as a function of time. (a) The mean number of neighbors of the same species for each lipid over simulation time in the DPPC-DIPC-Chol (30:58:12) mixture, without GM1 (red). In green is represented the total number of neighbors, whatever their nature. The cut-off distance $d = 13 \text{ \AA}$ was used to determine the neighbors of each lipid. (b) The mean number of neighbors of the same species fitted with $\langle n(t) \rangle = A - Be^{-t/\tau}$. This fit allows one to extract the typical equilibration time τ . One obtains τ of 2.8, 3.6, 6.6 and 5.6 μs for GM1 fractions in the upper leaflet of 0 (orange, the same as the red curve in (a)), 5% (red), 10% (purple) and 15% (blue) respectively.



relaxation time increases with the concentration of GM1, suggesting that the presence of GM1 slows down the phase separation process as observed previously.²² Thus, these results suggest that our systems can phase separate in between 5 μ s and 10 μ s as a function of the GM1 concentration.

3.1.2 Identification of Lo and Ld phases. Once phase-separated, we can identify the different phases by discretizing the membrane patches into a mesh of $N = L \times L$ boxes with $L = 15$ (each box is then of side $\delta x \simeq 3$ nm and contains at least one lipid). For DIPC and DPPC lipids, each phospholipid position is identified by the coordinates of the PO4 bead corresponding to the phosphate group while the GM1 positions are identified by the coordinates of the GM1 bead (Fig. 1a). The latter is located at an average depth similar to the phosphate groups in the upper leaflet as the two first sugar rings of GM1 can be deeply embedded in the interfacial region of the membrane.²² The local composition of a box can then be computed as the ratio of any molecules to the total number of molecules in the box (Fig. 5a and b). For DPPC molecules, the fraction of molecules in all boxes is sampled over all simulation frames and the threshold was set to a DPPC fraction of 0.6, where the composition distribution shows a marked minimum (Fig. 5c). The composition ratio is then regularly computed in each box along the course of the simulation and binarized with the threshold defined above so that the two phases are identified (Fig. 5d). We can now compute the observables of interest as a function of the local composition in the mesh and measure their correlations (see the ESI,† Section D).

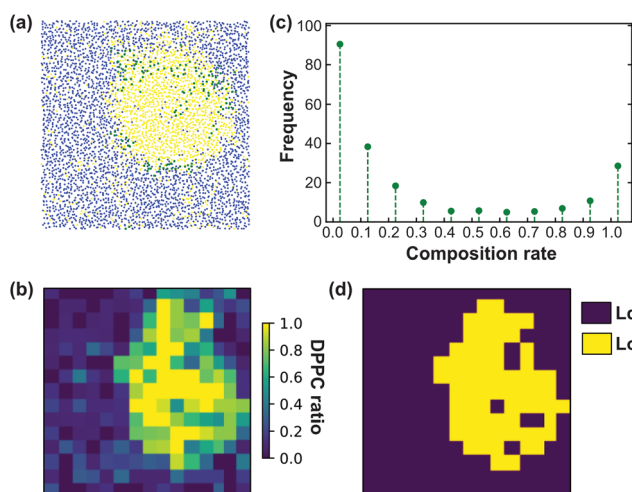


Fig. 5 Lo/Ld discretisation of the CG membrane model. (a) Illustration of the spatial distribution of the different lipid species for the last frame of the planar CG system (see Fig. 3). Each molecule position is identified by the position of one bead in the leaflet plane (see the text). DPPC is shown in yellow, DIPC in blue and GM1 in green. (b) Examples of analysis performed for a DPPC–DIPC–Chol (30 : 58 : 12) mixture with 10% GM1 in the upper leaflet (using a different snapshot as compared to in (a)). The bilayer is divided into a 15×15 mesh. (c) The composition distribution (fraction of DPPC in boxes of the bilayer, measured throughout the simulation time). (d) The composition repartition matrix in terms of DPPC ratio is binarized in Lo (yellow) and Ld (blue) boxes based on the composition distribution presented in c and according to the majority rule described in the text.

3.1.3 Localization of GM1. To begin with, we measure the relative ratios of GM1 molecules that are located in the Lo and Ld phases and at the Lo phase boundary, weighted by the corresponding area ratios (Fig. 6). We compute for instance the number of GM1 molecules in the Lo phase over the Lo domain area and divide it by the total number of GM1 molecules over the leaflet area. This confirms that in our simulations, the GM1 molecules preferentially partition into the Lo phase as observed experimentally in ref. 26. We conduct the same measurement for the GM1 molecules located in the Lo domain boundary zone in order to see whether GM1 is preferentially located at the boundary. Our results indicate that they are roughly homogeneously distributed in the domain (see also Fig. 3). Thereafter, the ensuing curvature is thus assumed to be quasi-uniform in the domain.

3.2 Calculation of parameters extracted from CG-MD simulations to accurately design the mesoscale model

Initial calculations allow us to calculate parameters extracted from CG simulations to be used as inputs for the mesoscale model (see the methods section). They are:

1. The bending moduli of both phases (κ_{Ld} and κ_{Lo}).
2. The two dimensionless spontaneous curvatures of the Ld and Lo + GM1 phases, denoted by RC_0 and $\text{RC}_{\text{Lo+GM1}}^{\text{vesicle}}$.
3. The Ising parameter J_1 (related to the line tension between both phases).
4. The relative timescales associated with diffusion in the membrane plane on the one hand and transverse deformation modes on the other hand, if one is interested in dynamical properties.

We explain below how to extract from CG simulations the values of these parameters, which are intrinsic to the molecular species at play (and their phase state through temperature). As the system needs at most around 8 μ s to equilibrate (see Fig. 4b), the following measurements are performed after 8 μ s, for a duration of 12 μ s (unless stated otherwise) so that phase separation is essentially reached.

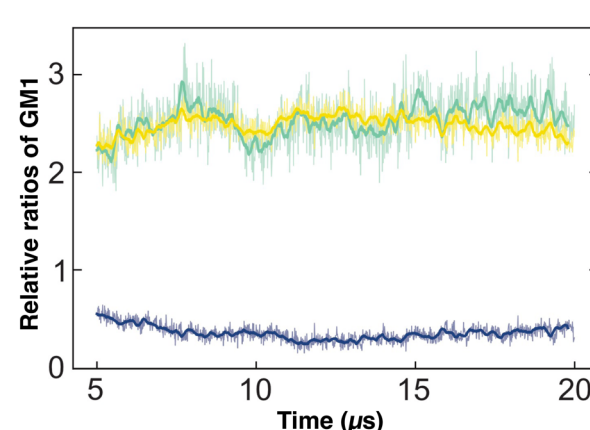


Fig. 6 Relative ratios of GM1 molecules located in the Ld (blue) and Lo (yellow) phases and at the Lo phase boundary (green) weighted by the corresponding area ratios. DPPC–DIPC–Chol (30 : 58 : 12) mixture with 10% GM1 in the upper leaflet.



Two other parameters are important for membrane patterning:^{19,43,62}

- The membrane surface tension σ
- The area fraction of each phase (ϕ is the fraction of the Lo + GM1 phase and $1 - \phi$ the fraction of the Ld phase, both conserved through time)

These extrinsic parameters depend on the experimental conditions and are not extracted from the CG simulations.

3.2.1 Determination of bending moduli of both phases κ_{Ld} and κ_{Lo} . The bending modulus values of both Ld and Lo phases, respectively κ_{Ld} and κ_{Lo} , must be set as parameters in the mesoscale model.

Generically, ref. 63 has shown how the bending modulus κ of a bilayer made of a homogeneous lipid mixture can be inferred from the spectral density of the membrane thermal shape fluctuations in CG simulations using the Helfrich model for membranes. In our CG simulations, the surface tension was set to $\sigma = 0$, to make the determination of κ easier. However, the continuous Helfrich model ignores short-wavelength molecular scales where individual lipids jiggle out of the local membrane plane, forming some “protrusions”.^{64–66} Assuming that protrusions and Helfrich fluctuations are independent random variables, one obtains the spectral density of fluctuations in the Fourier space⁶⁷

$$\langle |\hat{h}(\mathbf{q})|^2 \rangle = L^2 k_{\text{B}} T \left(\frac{1}{\kappa q^4} + \frac{1}{\sigma_{\text{pr}} q^2} \right) \quad (12)$$

where σ_{pr} is the protrusion tension, measured to be $\sigma_{\text{pr}} \sim 0.1 \text{ J m}^{-2}$ on simple coarse-grained numerical membrane models.^{64,65} Protrusions dominate the spectral density of fluctuations for wavevectors $q \geq \sqrt{\sigma_{\text{pr}}/\kappa}$, *i.e.* at wavelengths $2\pi/q \leq 4 \text{ nm}$ when $\kappa \sim 10 k_{\text{B}} T$. Thus one must use large enough system sizes L to reliably measure κ , as well as long simulation times to reduce statistical errors.

We performed these measurements on our own CG simulations of Ld and Lo membranes, by using the approach in ref. 63. Fitting with eqn (12), we estimated the values of κ for both systems, $\kappa_{\text{Ld}} = 13 k_{\text{B}} T$ for the Ld phase, and $\kappa_{\text{Lo}} = 25 k_{\text{B}} T$ for the Lo one (see the ESI,† Section B, for further details).

3.2.2 Determination of the spontaneous curvature of the Lo phase. In order to compute the local curvature of the upper leaflet for the different phases of the CG model, as the membrane exhibits only small bending, we approximate the total curvature by using a 2D (discrete) Laplacian $\tilde{\Delta}$, using the four nearest neighbors, applied on the height field:

$$\tilde{\Delta}h_{k,\ell} = \frac{h_{k+1,\ell} + h_{k-1,\ell} + h_{k,\ell+1} + h_{k,\ell-1} - 4h_{k,\ell}}{\delta x^2} \quad (13)$$

Here $h_{k,\ell}$ is the height of the membrane on the box of integer coordinates (k,ℓ) on the 15×15 mesh defined above, endowed with periodic boundary conditions. Note that we choose to measure the curvature of the upper leaflet because we are primarily interested in the curvature generated by GM1 insertions in this leaflet.

The Lo phase, where GM1 molecules are mainly inserted, as shown in Fig. 6, displays a higher curvature than the Ld one

(Fig. 7a and b). This Lo domain curvature increases with the addition of GM1 molecules (Fig. 7c). We notice that for 0% of GM1, the Lo domain has a weak curvature. This upper leaflet weak curvature results from the difference in thickness in between the Lo and Ld domains and the fact that the leaflet position is identified through the positions of the PO4 and GM5 beads (see above).

Note that because of the periodic boundary conditions, the total curvature averaged on the whole system mathematically vanishes when it is approximated by a Laplacian. Thus if the Lo phase is curved, the Ld phase must be curved as well in the opposite direction, so that the average curvature is zero (Fig. 7d).

To quantify how GM1 molecules affect upper leaflet curvature, we plot (the absolute value of) the difference in curvature $C_{\text{Lo+GM1}}^{\text{planar}}$ between the Lo domains enriched in GM1 and the small reference curvature ($|C| \simeq 0.0087 \text{ nm}^{-1}$) of the Lo domain without GM1 insertions (Fig. 8). The curvature values are averaged from 10 to 20 μs on the measurements shown in Fig. 7c to ensure that they are extracted from equilibrated domains. We find that $C_{\text{Lo+GM1}}^{\text{planar}}$ depends linearly on the GM1 fraction as

$$C_{\text{Lo+GM1}}^{\text{planar}} \simeq 0.5 \phi_{\text{GM1}} \text{ nm}^{-1} \quad (14)$$

This linear law is in agreement with the results of ref. 30 finding a comparable slope in their MD simulations, even though they have used another type of coarse-grained model.

Below, we want to model non-planar systems (*i.e.* vesicles) with our mesoscale model. We denote using C_0 the spontaneous curvature of the Ld phase. In the present case, $C_0 = 2/R$ is set by the vesicle average radius R in equilibrium, to accommodate the area difference between both leaflets.⁶⁸ We recall that we also denote by $C_{\text{Lo+GM1}}^{\text{vesicle}}$ the spontaneous curvature of the Lo + GM1 phase on a vesicle. On a vesicle, we can also assume that before insertion of GM1, the Lo phase has the same curvature $C_0 = 2/R$, for the same reason as for the Ld phase, so that the GM1 curvature comes in addition to C_0 as examined in detail in ref. 68. Thus $C_{\text{Lo+GM1}}^{\text{vesicle}} = C_0 + C_{\text{Lo+GM1}}^{\text{planar}}$ where $C_{\text{Lo+GM1}}^{\text{planar}}$ is given in eqn (14). A more thorough discussion about this relationship is provided in the ESI,† Section A.

3.2.3 Determination of the Ising parameter through measurement of the line tension. As explained in the Methods section, one can relate the line tension λ of the boundary between the Lo and Ld phase extracted from CG-MD simulations and the Ising parameter J_{I} of the mesoscale model. This relationship ensues from the critical behavior of the mixture near its phase transition. Close enough to the critical value $J_{\text{I,c}}$, we have (eqn (11)):

$$\lambda = \frac{4\sqrt{3}}{a} (J_{\text{I}} - J_{\text{I,c}}) \quad (15)$$

from which it follows that

$$J_{\text{I}} = J_{\text{I,c}} + \frac{a\lambda}{4\sqrt{3}} = \frac{\ln 3}{4} k_{\text{B}} T + \frac{a\lambda}{4\sqrt{3}} \quad (16)$$

The measurement of λ thus gives access to the mesoscale Ising parameter J_{I} . Note that when one goes away from $J_{\text{I,c}}$, non-linear



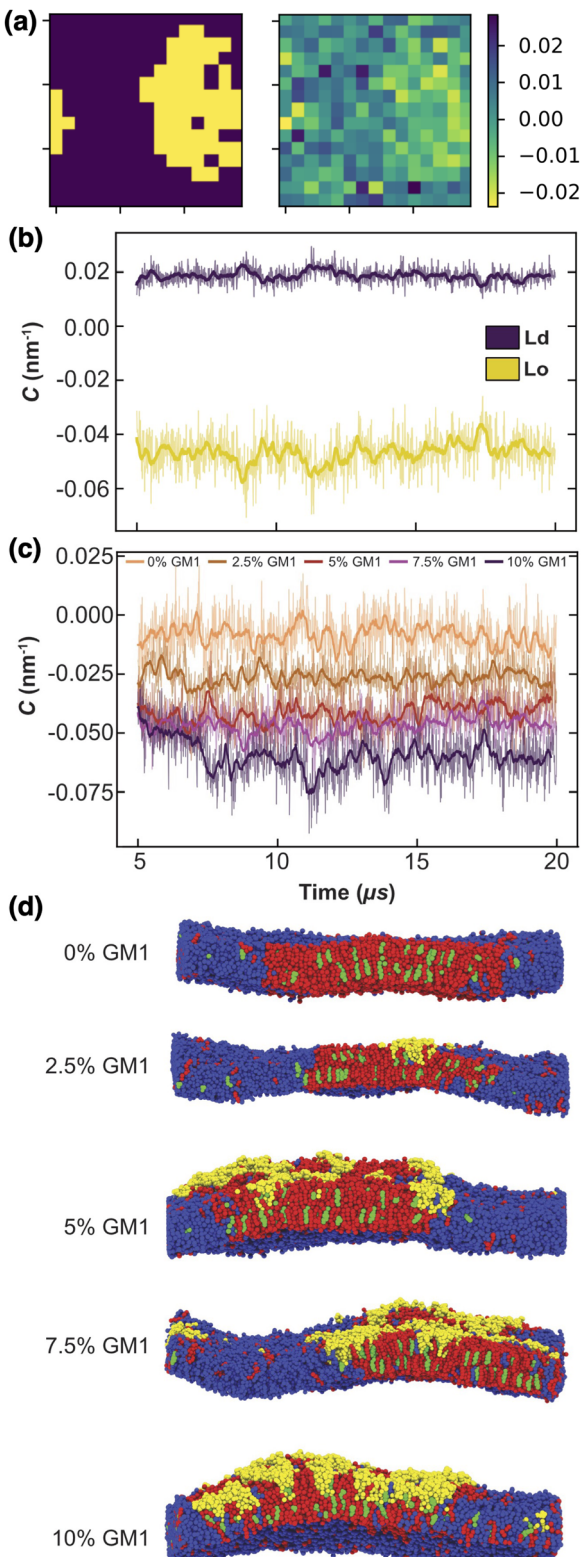


Fig. 7 The local curvature imposed by GM1 molecules. (a) The local curvature (right, in nm^{-1}) against the lipid phase (left). (b) The local curvature measurement through time, averaged for the Lo and Ld phase separately, in the upper leaflet for a DPPC–DIPC–Chol mixture with 7.5% GM1 in the upper leaflet. (c) Curvature of the Lo phase from 0 to 10% GM1 in the upper leaflet (by increments of 2.5) from orange to purple. This curvature is negative because of our sign convention in eqn (13). (d) Side views of the different systems at 20 μs .

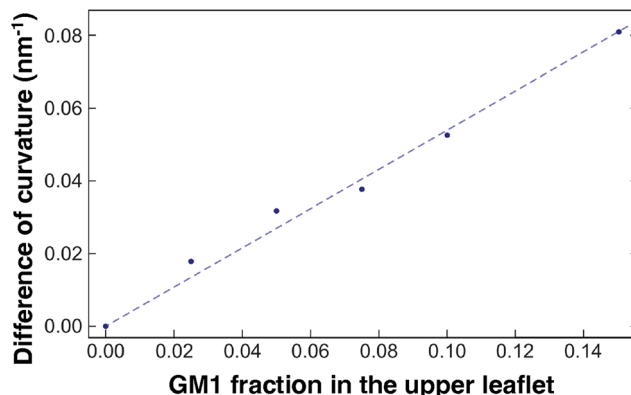


Fig. 8 The correlation between curvature and GM1 concentration. The difference in curvature $C_{\text{Lo+GM1}}^{\text{planar}}$ between the Lo domain with GM1 and the reference Lo domain without GM1 in planar geometry. The curvature values are averaged on the last 10 μs . The DPPC–DIPC–Chol (30 : 58 : 12) mixture with a growing fraction of GM1 in the upper leaflet, and the linear fit given in eqn (14) (dashed line).

subdominant terms come into play.³³ We assume that this approximation provides reasonable estimates of J_1 in the present case. Analytical^{47,55} or numerical solutions can also be used far from the critical point.

To measure the line tension λ at the boundary of Lo and Ld phases in a mixture devoid of GM1, we measure the fluctuations of the Lo domain boundary. We use the same method as the one applied to fluorescence microscopy images in ref. 53 or in mesoscale simulations.⁶⁹ We use the polar discretization (detailed in the methods section) in order to identify the location $r(\theta)$ of the Lo + GM1 domain boundary, the origin of coordinates being the domain barycenter. We then apply the DPPC fraction threshold of 0.6 (Fig. 5c) to delineate the boundary between Lo and Ld domains and calculate the Fourier coefficients u_n of $u(\theta)$, defined by $r(\theta) = R_0[1 + u(\theta)]$, using a fast Fourier transform algorithm. Finally, we use eqn (8) to relate the power spectrum of the boundary fluctuations to the line tension of the domain boundary $\langle |u_n|^2 \rangle$ against $1/(n^2 - 1)$. We fit only the first long wavelength modes to avoid discretization effects, as shown in Fig. 9. The fitted line tension is $\lambda \simeq 3$ pN for a DPPC–DIPC–Chol (30 : 58 : 12) mixture devoid of GM1 at $T = 310$ K, of the same pN order of magnitude as the experimental values.¹⁹

We also measured how λ depends on the GM1 concentrations, as shown in Table 3. In agreement with the CG simulations in ref. 21, λ decreases when the GM1 concentration increases above 5%, resulting in an increased width of the phase boundary, which appears less regular in Fig. 3. Indeed, the width of the phase boundary is set by the spatial correlation length ξ , itself inversely proportional to λ in the 2D Ising universality class⁴⁷ where $\lambda\xi = k_B T$.

3.2.4 Determination of vertex-composition diffusion timescale. Here, we focus on dynamic questions that do not concern equilibrium properties of phase separation. Indeed convergence to equilibrium only relies on the detailed balance condition,⁴⁸ and not on the exact values and physical relevance



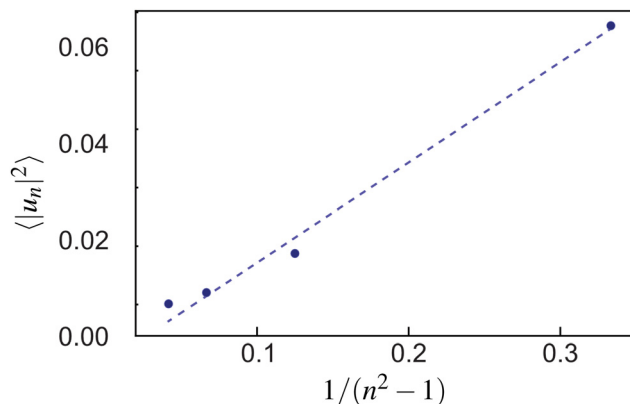


Fig. 9 The power spectrum of the Lo-Ld boundary in a DPPC–DIPC–Chol mixture without GM1 from which the line tension λ is extracted through a fit with eqn (8) (dashed line).

of the Monte Carlo transition rates in the simulation framework. A reader interested only in equilibrium issues can skip this section.

In the mesoscale model, the rate at which vertex-composition flips (Kawasaki dynamics, see the methods section) are attempted must be set by a relevant timescale δt at the length scale a , the average lattice spacing. This is related to the diffusion coefficient D of the minority species in the bulk of the majority phase at this scale, through the relationship $a^2 = 4D\delta t$. Here, we also show how D can be inferred from the measurement of the line tension λ in CG-MD simulations. However, the effective value of D also depends on the mesoscopic length scale a , as we discuss it now. Note that D cannot simply be set as the diffusion coefficient of molecules in the bilayer because a membrane patch at the mesoscale can be a collection of dozens of lipids, or even more. Its diffusive properties are the fruit of the collective behavior of its interacting elementary constituents, themselves in interaction with the surrounding fluid.

Domain boundary fluctuations are known to be a relevant probe of diffusion in phase-separated membranes.^{53,70,71} A notorious difference can already be noticed between our mesoscopic modeling on the one hand and MD simulations or experiments on the other hand. While hydrodynamic interactions are absent in the former due to the construction of our MC simulations, they are intrinsically present in the latter where the solvent is explicitly simulated (note however that accounting for hydrodynamic interactions in Monte Carlo simulations in general⁷² and in membrane modeling in particular is feasible in principle,^{73,74} at least as far as homogeneous membranes are concerned). This implies different scaling laws of the timescales as a function of the length scales.

Table 3 Measured line tensions λ as a function of the GM1 concentration in the upper leaflet

% GM1	0	2.5	5	7.5	10	15
λ (pN)	3.0	3.0	5.0	2.4	1.2	0.8

Ref. 70 and 71 thoroughly address the role of hydrodynamic interactions in this context, in the frame of the Saffman–Delbrück theory. One can define a typical length, the Saffman–Delbrück length $L_{SD} = h\eta_m/(2\eta_f)$, where η_m and η_f are the viscosities of the membrane and the fluid, respectively, and h is the membrane thickness. L_{SD} is on the order of 100 nm to 10 μ m in experimental systems. On length scales below L_{SD} , 2D hydrodynamics inside the membrane dominates, while above it, 3D hydrodynamics in the surrounding solvent dominates. Considering a boundary fluctuation wavelength Λ , it follows that its relaxation time scales as $\tau(\Lambda) \propto \Lambda^2$ if $\Lambda \gg L_{SD}$ and $\tau(\Lambda) \propto \Lambda$ if $\Lambda \ll L_{SD}$. In the ESI,† Section F, we properly define the relaxation times and we discuss these relationships. Below, we focus on (nanometric) values of $\Lambda \ll L_{SD}$ at the molecular scale, so that

$$\tau_{MD}(\Lambda) = \frac{2h\eta_m}{\pi\lambda}\Lambda \quad (17)$$

where λ still denotes the line tension.

Our choice to set the value of D in mesoscale simulations consists in identifying the molecular and mesoscopic time scales at the smallest wavelength accessible in the mesoscale model, namely $\Lambda = 2a$.‡ This means that we assume here that hydrodynamic interactions are at play up to the length scale a only. Since hydrodynamics interactions are known to enhance dynamics⁷⁵ it implies that the larger a , the faster the dynamics at large scales, thus the larger effective D , as we quantify it now.

In the mesoscale simulations where no hydrodynamic interactions are at play and where the order parameter is conserved, it can be demonstrated⁷⁶ that the relaxation time at wavelength Λ is related to the diffusion coefficient D through

$$\tau_{Meso}(\Lambda) = A \frac{\lambda}{D J_1} \Lambda^3 \quad (18)$$

where A is a dimensionless constant that was determined numerically on the triangular lattice, $A \simeq 0.1$. The identity $\tau_{MD}(2a) = \tau_{Meso}(2a)$ finally sets the value of the diffusion coefficient D , and therefore the timescale $\delta t = a^2/(4D)$ under interest. Here we need the value of J_1 , which also depends on a . It can be estimated through the approximation in eqn (16). We eventually get

$$D \simeq 2\pi A \frac{\lambda^2 a^2}{h\eta_m} \frac{4}{k_B T \ln 3 + a\lambda/\sqrt{3}} \quad (19)$$

As expected, this diffusion coefficient D in the membrane plane depends on a . It also depends on λ that can be measured using CG-MD simulations, as explained above. We emphasize that this relationship simply reflects our choice to get the timescales at length scale $2a$ to coincide. In this expression, the line tension λ expresses the role of the interactions between the molecular constituents.

‡ Indeed, the circumference of a circular domain of radius R_0 is discretized into $N_R \simeq 2\pi R/a$ elementary edges of the sphere tessellation. The discrete Fourier transform of the boundary fluctuations is written with Fourier coefficients u_n associated with wavelengths $2\pi R/n$ (see the methods section), n running from $-N_R/2 + 1$ to $N_R/2$. Hence the smallest accessible wavelength is $2\pi R/(N_R/2) = 2a$.

Given that dynamics are known to be significantly enhanced in MD simulations using the MARTINI force field^{77–79} (see also the ESI,† Section F), we prefer to use experimental values of η_m rather than numerically measured ones. In the present case, we estimate in the SI that $h\eta_m \simeq 4 \times 10^{-10}$ Pa.m.s. For instance, for a vesicle of radius $R = 30$ nm as considered below, the average tessellation edge length is $a = 2.25$ nm for $N = 2562$ vertices. With the measured value $\lambda \approx 0.8$ pN at 15% of GM1 in the upper leaflet, and $T = 310$ K, we get the numerical values $D \approx 3.6 \mu\text{m}^2 \text{s}^{-1}$ and finally $\delta t \approx 0.35 \mu\text{s}$. The value of D is lower than the lipid diffusion coefficients measured in real model membranes, *e.g.* vesicles,⁸⁰ although they are on the same order of magnitude because with this value of R , the patches are small, and each vertex represents about 6 lipid molecules in each leaflet.

In the ESI,† Section G, the value of δt , associated with diffusion in the membrane plane, is compared to its transverse counterpart δt_p , the physical timescale associated with (one-dimensional) radial MC moves. With the same model parameters as above, one obtains $\delta t_p = 90$ ps, which is much shorter than δt . This means that if one were interested in studying realistic vesicle dynamics through kinetic Monte-Carlo simulations,⁴⁸ one would need to execute a large number of vertex radial moves in-between two vertex-composition flips, on the order of $\delta t/\delta t_p \approx 4000$. This ratio depends on the value of the vesicle radius R through several parameters.

3.3 Mesoscale simulation

Relying on the numerical results at the coarse-grained scale and after the extraction of the key parameters, we perform the mesoscale Monte Carlo simulation of a tessellated vesicle made of two phases, one corresponding to the Ld phase, the other one, with a higher spontaneous curvature, accounting for the Lo phase curved by GM1 insertions. We simulate a vesicle with $N = 2562$ vertices. Since our objective is to come back later to the CG scale through backmapping, we shall focus here on a small unilamellar vesicle (SUV). Details of the mesoscale numerical scheme are given in ref. 42 and 43, and summarized in the methods section.

As notably discussed in ref. 43, coarse-graining up to the mesoscale is a quantitative process which consists in pre-averaging the degrees of freedom at length-scales smaller than the lattice spacing a , the physical foundations of which are prescribed by the renormalization group theory.^{33,46} Consequently, one expects the mesoscale model to describe correctly the fluctuations of the real system at large scales, with the advantage that it will reach equilibrium much faster in terms of computational time, provided, as described just above, that microscopic details have been correctly integrated out in the mesoscale parameters. Note that in the same spirit, force fields used in all-atom or CG models have already integrated out electronic degrees of freedom, and are consequently already approximate.

As explained above, we use the following parameter values to simulate a vesicle of real radius $R = 30$ nm with the same Ld and

Lo + GM1 phases as in the bilayer with 15% of GM1 in the upper leaflet studied above:

1. The bending moduli are set to $\kappa_{\text{Lo}} = 25 k_{\text{B}}T$ and $\kappa_{\text{Ld}} = 13 k_{\text{B}}T$ after calculation of the membrane fluctuation spectra in the CG model.

2. The spontaneous curvature of the Ld phase is equal to $C_0 = 2/R$, the one of the average sphere. The spontaneous curvature of the Lo + GM1 phase is fixed to $C_{\text{Lo+GM1}}^{\text{vesicle}} = C_0 + C_{\text{Lo+GM1}}^{\text{planar}} = 4.43/R$, from measurements of $C_{\text{Lo+GM1}}^{\text{planar}}$ in CG simulations at 15% of GM1, as explained above.

3. The Ising parameter is set to $J_1 = 0.336 k_{\text{B}}T$ to match the measured line tension λ , through eqn (15). This value is above the critical one $J_{1,c} = (\ln 3/4)k_{\text{B}}T \simeq 0.275 k_{\text{B}}T$ on a triangular lattice.

4. The surface tension is arbitrary since it is an extrinsic parameter imposed by experimental conditions, and not a property of the membrane. In the simulations, its dimensionless value $\tilde{\sigma} = \sigma R^2/(k_{\text{B}}T)$ was set at 1100, which corresponds to $\sigma = 5.3 \times 10^{-3} \text{ J m}^{-2}$ for a radius $R = 30$ nm. This value ensures it is the quasi-spherical vesicle regime, where our mesoscale model is fully valid.⁴²

5. The area fraction ϕ of the Lo + GM1 phase is chosen equal to 20%, so that Lo domains are well-defined. Increasing this value would lead to more complex interdigitated, labyrinthine patterning.⁴³

The system was run for a long time (10^{10} MC steps) to ascertain that thermodynamic equilibrium has been reached.⁴³ A snapshot by the end of the simulation is displayed in Fig. 10.

With the parameters inferred from the CG model, the SUV displays nanodomains in equilibrium. As observed in previous work,⁴³ the domains form rapidly after starting the simulation from a configuration where Ld and Lo vertices were randomly distributed. Then the domains fluctuate in size and shape, permanently exchanging Lo “monomers” with the surrounding phase. They can also coalesce or split. It must be emphasized that as compared to the CG simulations above where a single nanodomain, necessarily smaller than the simulated box size, was formed in few μs on the quasi-flat membrane due to phase separation, the full phase separation displaying a single, large Lo domain, is avoided on the curved SUV, by introducing a surface tension, σ . Hence, the nanodomain size is controlled by the typical length scale λ/σ , since larger curved domains have a too large surface free-energy.¹⁹ The nanodomains are not generically larger (in real size) than in the CG simulations, but they never coalesce in a single, large Lo region.

To quantify this vesicle meso-patterning, we computed the nanodomain size-distribution, as illustrated in Fig. 10. As compared to distributions generally observed on large GUVs below the critical temperature (see the ESI† or ref. 43 for examples), the distribution is not bimodal but monotonously decreasing. The main reason for this difference is that on a SUV, the ratio between the Lo domain curvature $C_{\text{Lo+GM1}}^{\text{vesicle}}$ and the sphere one C_0 is moderate as compared to a GUV. The mesoscale model thus predicts that nanodomains on SUVs can dynamically adopt a wide range of sizes, from very small to



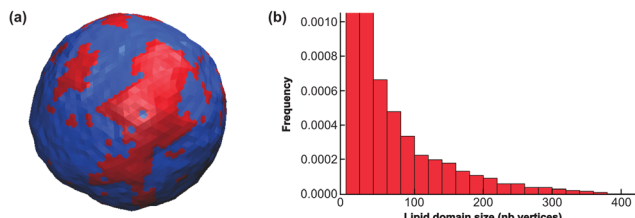


Fig. 10 Lipid nano domain sizes for the mesoscale model. (a) Snapshot of a mesopatterned SUV of radius 30 nm after equilibration through the mesoscale model. The area fraction ϕ of the Lo + GM1 curving phase (in red) is equal to 20%, which is to say there are 512 red vertices out of 2562 vertices (each vertex is represented here by 6 small triangles defining its Voronoi cell. For one given vertex the 6 triangles are all either red or blue). Other parameters are given in the text. (b) Nanodomain size distribution. Nanodomain sizes are given as the number of vertices in a given (Lo + GM1)-phase nanodomain. The two first bars have been truncated for clarity.

very large (with respect to the number of available Lo vertices) ones, that however never reach the maximum allowed size of 512.

3.4 Backmapping from the mesoscale model to the CG one

Backmapping from the mesoscale model to the CG system consists in decorating the elementary triangles of the mesoscale tessellation while respecting both the bilayer geometry and its local composition⁹ (see the methods section). The triangles are decorated with the same Ld and Lo + GM1 phases as in the bilayer with 15% of GM1 in the upper leaflet studied above with the help of CG simulations. The interior and exterior of the $R = 30$ nm-radius vesicle are filled with water (and ions) in order to constrain the vesicle interior volume as in the mesoscale simulation. Backmapping is exemplified in Fig. 11. We shall now verify that after backmapping from the mesoscale model to the CG one, CG simulations run from the so-obtained simulation output are stable through time, which will support the fact that the mesoscale parameters were correctly estimated. Whereas simulations at the mesoscale enable one to equilibrate the slow long wave-length fluctuations, above the lattice spacing a , at the price of ignoring the short wavelengths, CG simulations after backmapping enable one to equilibrate in turn these short, fast wavelengths, and finally to obtain a CG system equilibrated at all wavelengths, whereas equilibrating

long wavelengths with the help of the sole CG model would be prohibitive in terms of computational cost.

First, we have checked that at the molecular scale, backmapping reproduces faithfully lipid-tail ordering in both phases, by computing the usual acyl-chain order parameter in both systems with GM1 (see the ESI[†] Section H).

Then, in order to assess the supramolecular stability of the backmapped CG vesicle, notably in terms of its nanopatterning, we have tracked the largest nanodomains along a 10 μ s-long CG simulation, as shown in Fig. 12a. In order to identify unambiguously the Lo nanodomains, we have radially projected the lipid coordinates onto a regularly tessellated sphere made of 5120 elementary triangles and attributed the Lo or Ld nature to each of them by using the same kind of majority rule as previously, as shown in Fig. 5. We have measured that the total number of Lo triangles remains remarkably stable through time, very close to the initial 20% fraction before backmapping (see Fig. S6 in the ESI[†]). Furthermore, nanodomains are identified as the connected components of the Lo phase. As expected, the size of the largest nanodomains fluctuates, as they regularly lose or gain lipids of the Lo phase, however their size does not evolve much with time (see Fig. 12b). This suggests that the nanopatterning ensuing from the mesoscale simulation remains qualitatively stable with time and validates our whole multiscale scheme.

4 Discussion

This work proposes a complete strategy to extract valuable parameters from coarse-grained simulations to design a mesoscale model of biphasic vesicles. Going from the molecular scale to mesoscopic scales can present intrinsic difficulties, that we have fully addressed here, appealing to important physics concepts such as the renormalization group theory. This concerns in particular the scale-dependent relationship between the line tension at the interface between both phases, which is measured in CG simulations through the fluctuation spectrum of the interface between both phases, and controlled by the Ising parameter J_1 in the mesoscale model. Once equilibrated, the mesoscopic system is back-mapped to the molecular scale through a well-defined procedure. This multiscale simulation scheme eventually allows one to obtain large systems equilibrated at all length scales, which could not be achieved solely at the CG scale due to the prohibitive simulation time it would require. In particular, modeling at the mesoscale enables equilibration of long length scales before equilibration of short ones after backmapping to the molecular scale. Equilibrating long length scales enabled us to sample accurately the domain size distribution. Here we have tackled an SUV of modest size (diameter of 60 nm) as a proof of concept, but there is no obstacle in principle to tackle larger systems for which real equilibration times can become very large, on the order of hours for a GUV.²⁷

One aspect of equilibration that is not apprehended in this work is equilibration between both leaflets, through lipid flip-flops.⁶⁸ Phospholipids flip-flops are rare events in CG

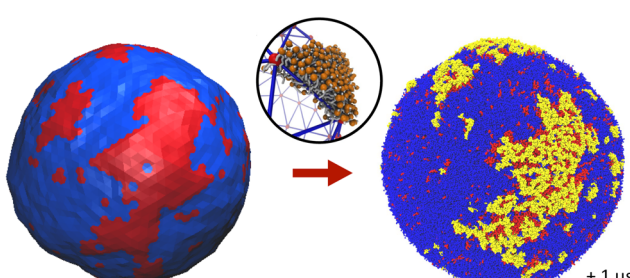


Fig. 11 Backmapping from the mesoscale model (left, equilibrated vesicle) to the CG one (right, after 1 μ s of CG simulation). The central circle image illustrates how each triangle of the tessellated vesicle is filled with a lipid bilayer patch.



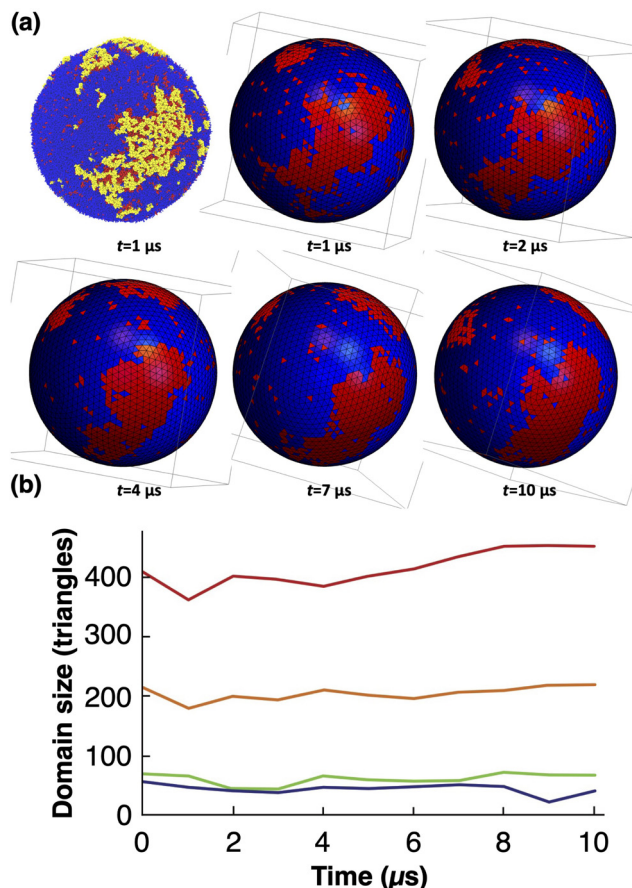


Fig. 12 Lipid Lo domains evolution in the CG-MD simulation. (a) CG-simulated vesicles projected onto the sphere and discretized again through the majority rule, at different simulation times. The first panel shows the CG vesicle at $t = 1 \mu\text{s}$, for comparison. The other frames have been rotated so that one can track the same lipid domains even though they diffuse slowly on the vesicle. (b) Domain size evolution with time (4 largest domains only). Note that the vesicle has twice as many triangles as vertices, so the largest domain, visible on the successive snapshots, contains about 200 vertices out of $N = 2562$.

molecular dynamics, with associated timescales on the order of hours, and they cannot be implemented in the mesoscale model that does not explicitly take leaflets into account. On timescales much shorter than the typical flip-flop time of interest here, the asymmetric distribution between leaflets is therefore considered to be metastable. At the mesoscale, this issue can in principle be solved by taking explicitly both leaflet compositions into account,⁴⁴ with stochastic composition exchanges between leaflets. In this case, note that the membrane spontaneous curvature would directly depend on these compositions.

In the present context, and in relation to the experiments of ref. 27, our CG simulations gave us new insights into the effect of insertion of the glycolipid GM1 into the Lo phase. Since GM1 is only inserted in one leaflet, the ensuing asymmetry imposes a local spontaneous curvature to the membrane, proportional to the concentration of GM1 in the leaflet. In addition, GM1 makes the Ld/Lo interface widen, which is a visual manifestation of the decrease in the interface line tension λ .

From a dynamical point of view, it also slows down the convergence to equilibrium. The two latter phenomena are intimately related since boundary fluctuation time-scales are inversely proportional to the line tension.⁷⁶ Increasing the spontaneous curvature of the minority phase while decreasing the line tension are both favorable to the stabilization of mesophases, where phase separation is incomplete in equilibrium, as observed in the mesoscale simulations. Note that the spontaneous curvature values imposed by GM1 are comparable to the spontaneous curvatures locally imposed by the insertion of some transmembrane proteins, measured by experimental or numerical techniques to be on the order of few 0.01 nm^{-1} .⁸¹⁻⁸⁴ Thus the meso-patterning effect observed at relatively large concentrations of GM1 is also expected to occur on cell membranes where curving proteins are abundant.¹⁹

Here we have used the Martini 2.2 forcefield. Recently, a new version of this forcefield was released increasing the number of bead types and sizes⁸⁵ refining diverse features especially related to the protein. This resulted in a recent reparametrization of carbohydrates⁸⁶ but a CG model of GM1 lipid has not yet been released. It will be interesting, in the coming years, to extend our CG modelling to see how this new version affects the quantitative results. In the meantime, the Martini 2.2 version has already given reasonable results^{21,22} on GM lipids and curvature to validate our proof of concept.

To perform our Monte Carlo mesoscale simulations, we used a model that some of us developed and characterized in recent studies.^{42,43} A more common model used in numerical statistical mechanics of membranes is the dynamically triangulated surface/membrane (DTS/DTM) model.^{51,52} Designed in the early 1990s to study the crumpling phase transition of homogeneous fluid membranes,^{87,88} it has been extended and enriched in order to model membranes or vesicles closer to cell membranes, in particular by endowing it with multiphasic composition.^{1,49} In our model, the vertices of the tessellation experience only radial moves and there are no edge-flips, which are an important characteristic of the DTS model.

These features do not modify in depth the overall properties of the model, however using our own model presents at least two advantages in the present context. First, as far as the Ising model is concerned, it dwells on a triangular lattice (except for the 12 vertices that have only 5 neighbors, necessary to close the membrane, due to Euler's polyhedron formula), whereas in the DTS case, it would dwell on a disordered lattice, with vertices that can have in principle any number of neighbors larger than 3. The rigorous connection between the line tension and the Ising parameter J_1 relies on the knowledge of the critical parameter $J_{1,c}$ and of the prefactor $4\sqrt{3}$ in eqn (15), whereas they are not exactly known on a disordered lattice. The same problem arises when it comes to diffusion and dynamical issues, as in eqn (19). Second, in the DTS model, edge lengths are constrained by an upper and a lower bound, in order to ensure membrane self-avoidance and to prevent some triangles from becoming very large to the detriment of the smallest ones. Because of entropic effects due to these constraints in the configuration space, an additional entropic term modifies the



input surface tension σ in a way that is difficult to control because it depends in a non-trivial way on the total area of the vesicle. The quantification of this effect is out of the scope of this work and will be the object of a forthcoming publication. For these reasons, we did not opt for the DTS model in the present study where every mesoscale parameter must be well-controlled.

The membrane surface tension is one of the key parameters of the mesoscale model because the topology of the meso-pattern⁸⁹ and even its stability depend on the surface tension value. A large enough value is required to destabilize the macrophase whereas a too large value would suppress membrane fluctuations and thus also lead to macrophase separation.^{19,43,62} When backmapping to CG simulations, the surface tension can easily be monitored in planar geometry by applying anisotropic pressure on the simulation box.⁷⁷ However, controlling the surface tension is more challenging in vesicle geometry.⁹⁰ Indeed, it depends on the quantity of water and ions encapsulated inside the vesicle, due to the Laplace law, through the difference in pressure across the membrane. In this work, we have not quantified the surface tension of the vesicle after backmapping, but simply filled the vesicle with the maximum quantity of water (plus ions), anticipating that since the overall interior volume was the same as in the mesoscale vesicle simulations, the surface tensions should be comparable. Since it is difficult to compute *a priori* the value of the surface tension, the most obvious way to control it is to proceed by trial and error, removing water and ions if the tension is too high and adding ones if it is too weak, for example by pushing the existing solvent away from the center of the vesicle through application of a radial force. This issue will be addressed in the near future.

In the era of exascale computing,^{91,92} it is tempting to design molecular systems to study from organelles^{9,93} to viruses^{93,94} or even an entire cell.^{95–97} Yet, the computing power necessary to simulate such large systems is still very huge and prevents one from reaching simulated timescales useful to decipher even simple phenomena such as the diffusion of large molecules⁹³ without even mentioning relevant biological time scales of milliseconds or longer. Our approach may help in tackling this issue by equilibrating a simplified triangulated version of such huge systems using Monte Carlo simulations to then only refine the equilibrated system on nano- to micro-second timescales.

Author contributions

J. C. performed the simulations and analyzed the results. N. C. contributed to the analyses and M. P.-M. contributed to the CG simulations. M. C., W. P. and S. J. M. contributed to the simulations and result analyses. M. M., M. C. and N. D. designed and supervised the research. J. C., N. D., M. C. and M. M. wrote the manuscript.

Conflicts of interest

There are no conflicts to declare.

Acknowledgements

M. C. is supported by the CNRS-MITI grant “Modélisation du vivant” 2020 and by the ITMO Cancer of Aviesan “Mathématiques et Informatique”. This work was granted access to the HPC resources of CALMIP supercomputing center (under the allocation 2021-P21020) and TGCC Joliot-Curie supercomputer (under the GENCI allocation A0110712941). W. P. acknowledges funding from the Novo Nordisk Foundation (grant No. NNF18SA0035142) and Independent Research Fund Denmark (grant No. 10.46540/2064-00032B). M. M. and N. D. are affiliated with the Université Toulouse III-Paul Sabatier and the Centre National de la Recherche Scientifique (CNRS).

References

- W. Pezeshkian, M. Konig, S. J. Marrink and J. H. Ipsen, *Front. Mol. Biosci.*, 2019, **6**, 59.
- H. I. Ingólfsson, *et al.*, *Proc. Natl. Acad. Sci. U. S. A.*, 2022, **119**, e2113297119.
- H. I. Ingólfsson, H. Bhatia, F. Aydin, T. Oppelstrup, C. A. López, L. G. Stanton, T. S. Carpenter, S. Wong, F. D. Natale, X. Zhang, J. Y. Moon, C. B. Stanley, J. R. Chavez, K. Nguyen, G. Dharuman, V. Burns, R. Shrestha, D. Goswami, G. Gulten, Q. N. Van, A. Ramanathan, B. V. Essen, N. W. Hengartner, A. G. Stephen, T. Turbyville, P.-T. Bremer, S. Gnanakaran, J. N. Glosli, F. C. Lightstone, D. V. Nissley and F. H. Streitz, *J. Chem. Theory Comput.*, 2023, **19**, 2658–2675.
- O. N. Vickery and P. J. Stansfeld, *J. Chem. Theory Comput.*, 2021, **17**, 6472–6482.
- E. Lyman, H. Cui and G. A. Voth, *Phys. Chem. Chem. Phys.*, 2011, **13**, 10430–10436.
- T. A. Wassenaar, K. Pluhackova, R. A. Böckmann, S. J. Marrink and D. P. Tieleman, *J. Chem. Theory Comput.*, 2014, **10**, 676–690.
- T. D. Newport, M. S. P. Sansom and P. J. Stansfeld, *Nucleic Acids Res.*, 2018, **47**, 1362–4962.
- Y. Peng, A. J. Pak, A. E. P. Durumeric, P. G. Sahrman, S. Mani, J. Jin, T. D. Loose, J. Beiter and G. A. Voth, *J. Phys. Chem. B*, 2023, **127**, 8537–8550.
- W. Pezeshkian, M. Konig, T. A. Wassenaar and S. J. Marrink, *Nat. Commun.*, 2020, **11**, 2296.
- W. Pezeshkian and S. J. Marrink, *Curr. Opin. Cell Biol.*, 2021, **71**, 103–111.
- M. N. Melo, H. I. Ingólfsson and S. Marrink, *J. Chem. Phys.*, 2015, **143**, 243152.
- S. A. Shelby, I. Castello-Serrano, K. C. Wisser, I. Levental and S. L. Veatch, *Nat. Chem. Biol.*, 2023, 1–9.
- S. L. Veatch, P. Cicuta, P. Sengupta, A. Honerkamp-Smith, D. Holowka and B. Baird, *ACS Chem. Biol.*, 2008, **3**, 287–293.
- T. Lang and S. Rizzoli, *Physiology*, 2010, **25**, 116–124.
- H. I. Ingólfsson, M. N. Melo, F. J. V. Eerden, C. Arnarez, C. A. Lopez, T. A. Wassenaar, X. Periole, A. H. D. Vries, D. P. Tieleman and S. J. Marrink, *J. Am. Chem. Soc.*, 2014, **136**, 14554–14559.

16 E. Sezgin, I. Levental, S. Mayor and C. Eggeling, *Nat. Rev. Mol. Cell Biol.*, 2017, **18**, 361–374.

17 M. Cebecauer, M. Amaro, P. Jurkiewicz, M. Sarmento, R. Sachl, L. Cwiklik and M. Hof, *Chem. Rev.*, 2018, **118**, 11259–11297.

18 A. L. Duncan, R. A. Corey and M. S. P. Sansom, *Proc. Natl. Acad. Sci. U. S. A.*, 2020, **117**, 7803–7813.

19 N. Destainville, M. Manghi and J. Cornet, *Biomolecules*, 2018, **8**, 104.

20 D. Marsh, *Chem. Phys. Lipids*, 2010, **163**, 667–677.

21 R. Dasgupta, M. S. Miettinen, N. Fricke, R. Lipowsky and R. Dimova, *Proc. Natl. Acad. Sci. U. S. A.*, 2018, **115**, 5756–5761.

22 Y. Liu, J. Barnoud and S. J. Marrink, *Biophys. J.*, 2019, **117**, 1215–1223.

23 H. Ewers, W. Romer, A. E. Smith, K. Bacia, S. Dmitrieff, W. Chai, R. Mancini, J. Kartenbeck, V. Chambon, L. Berland, A. Oppenheim, G. Schwarzmann, T. Feizi, P. Schwille, P. Sens, A. Helenius and L. Johannes, *Nat. Cell Biol.*, 2010, **12**, 11–18.

24 M. Aureli, L. Mauri, M. G. Ciampa, A. Prinetti, G. Toffano, C. Secchieri and S. Sonnino, *Mol. Neurobiol.*, 2016, **53**, 1824–1842.

25 C.-L. Schengrund, *Trends Biochem. Sci.*, 2015, **40**, 397–406.

26 S. Sonnino, L. Cantù, M. Corti, D. Acquotti and B. Venerando, *Chem. Phys. Lipids*, 1994, **71**, 21–45.

27 S. F. Shimobayashi, M. Ichikawa and T. Taniguchi, *EPL*, 2016, **113**, 56005.

28 R. Bao, L. Li, F. Qiu and Y. Yang, *J. Phys. Chem. B*, 2011, **115**, 5923–5929.

29 J. Steinkühler, P. Fonda, T. Bhatia, Z. Zhao, F. S. C. Leomil, R. Lipowsky and R. Dimova, *Adv. Sci.*, 2021, **8**, 2102109.

30 A. Sreekumari and R. Lipowsky, *J. Chem. Phys.*, 2018, **149**, 084901.

31 A. Duncan and W. Pezeshkian, *Biophys. J.*, 2023, **122**(11), 1883–1889.

32 V. T. Ruhoff, P. M. Bendix and W. Pezeshkian, *Emerging Top. Life Sci.*, 2023, **7**, 81–93.

33 J. J. Amazon and G. W. Feigenson, *Phys. Rev. E: Stat., Nonlinear, Soft Matter Phys.*, 2014, **89**, 022702.

34 P. C. Hsu, B. M. H. Bruininks, D. Jefferies, P. C. T. D. Souza, J. Lee, D. S. Patel, S. J. Marrink, Y. Qi, S. Khalid and W. Im, *J. Comput. Chem.*, 2017, **38**, 2354–2363.

35 Y. Qi, H. I. Ingólfsson, X. Cheng, J. Lee, S. J. Marrink and W. Im, *J. Chem. Theory Comput.*, 2015, **11**, 4486–4494.

36 S. J. Marrink, H. J. Risselada, S. Yefimov, D. P. Tieleman and A. H. de Vries, *J. Phys. Chem. B*, 2007, **111**, 7812–7824.

37 M. J. Abraham, T. Murtola, R. Schulz, S. Pall, J. C. Smith, B. Hess and E. Lindahl, *SoftwareX*, 2015, **1–2**, 19–25.

38 G. Bussi, D. Donadio and M. Parrinello, *J. Chem. Phys.*, 2007, **126**, 014101.

39 M. Parrinello and A. Rahman, *J. Appl. Phys.*, 1981, **52**, 7182.

40 E. L. Wu, X. Cheng, S. Jo, H. Rui, K. C. Song, E. M. Dávila-Contreras, Y. Qi, J. Lee, V. Monje-Galvan, R. M. Venable, J. B. Klauda and W. Im, *J. Comput. Chem.*, 2014, **35**, 1997–2004.

41 R. J. Gowers, M. Linke, J. Barnoud, T. J. E. Reddy, M. N. Melo, S. L. Seyler, J. Domanski, D. L. Dotson, S. Buchoux, I. M. Kenney and O. Beckstein, *Proceedings of the 15th Python in Science Conference*, 2016, pp. 98–105.

42 G. Gueguen, N. Destainville and M. Manghi, *Soft Matter*, 2017, **13**, 6100–6117.

43 J. Cornet, N. Destainville and M. Manghi, *J. Chem. Phys.*, 2020, **152**, 244705.

44 G. Gueguen, N. Destainville and M. Manghi, *Eur. Phys. J. E: Soft Matter Biol. Phys.*, 2014, **37**, 76.

45 M. Meyer, M. Desbrun, P. Schröder and A. H. Barr, *Discrete differential-geometry operators for triangulated 2-manifolds*, Springer Berlin Heidelberg, Berlin, Heidelberg, 2003, pp. 35–57.

46 P. M. Chaikin and T. C. Lubensky, *Principles of condensed matter physics*, Cambridge University Press, 1995.

47 R. Baxter, *Exactly solved models in statistical mechanics*, Academic Press, 1982.

48 M. E. J. Newman and G. T. Barkema, *Monte Carlo Methods in Statistical Physics*, Oxford University Press, Oxford, New York, 1999.

49 J. Hu, T. Weikl and R. Lipowsky, *Soft Matter*, 2011, **7**, 6092–6102.

50 S. Penic, A. Iglic, I. Bivas and M. Fosnaric, *Soft Matter*, 2015, **11**, 5004–5009.

51 M. Siggel, S. Kehl, K. Reuter, J. Köfinger and G. Hummer, *J. Chem. Phys.*, 2022, **157**, 174801.

52 W. Pezeshkian and J. H. Ipsen, *Nat. Commun.*, 2024, **15**, 548.

53 C. Esposito, A. Tian, S. Melamed, C. Johnson, S.-Y. Tee and T. Baumgart, *Biophys. J.*, 2007, **93**, 3169–3181.

54 P. Flory, *Principles of polymer chemistry*, Cornell University Press, 1953.

55 V. A. Shneidman and R. K. P. Zia, *Phys. Rev. B: Condens. Matter Mater. Phys.*, 2001, **63**, 085410.

56 S. Safran, *Statistical thermodynamics of surfaces, interfaces, and membranes*, CRC Press, 2003.

57 C. Arnarez, J. J. Uusitalo, M. F. Masman, H. I. Ingólfsson, D. H. D. Jong, M. N. Melo, X. Periole, A. H. D. Vries and S. J. Marrink, *J. Chem. Theory Comput.*, 2015, **11**, 260–275.

58 W. Pezeshkian, F. Grünewald, O. Narykov, S. Lu, V. Arkhipova, A. Solodovnikov, T. A. Wassenaar, S. J. Marrink and D. Korkin, *Structure*, 2023, **31**, 492–503.e7.

59 E. Jefferys, M. S. P. Sansom and P. W. Fowler, *Faraday Discuss.*, 2014, **169**, 209–223.

60 H. J. Risselada and S. J. Marrink, *Proc. Natl. Acad. Sci. U. S. A.*, 2008, **105**, 17367–17372.

61 G. A. Pantelopoulos and J. E. Straub, *Biophys. J.*, 2018, **115**, 2167.

62 S. Weitz and N. Destainville, *Soft Matter*, 2013, **9**, 7804–7816.

63 P. W. Fowler, J. Hélie, A. Duncan, M. Chavent, H. Koldø and M. S. P. Sansom, *Soft Matter*, 2016, **12**, 7792–7803.

64 R. Goetz, G. Gompper and R. Lipowsky, *Phys. Rev. Lett.*, 1999, **82**, 221–224.

65 A. Imparato, J. C. Shillcock and R. Lipowsky, *Europhys. Lett.*, 2005, **69**, 650–656.

66 F. Schmid, *Biophys. Rev. Lett.*, 2013, **08**, 1–20.

67 H. Shiba and H. Noguchi, *Phys. Rev. E: Stat., Nonlinear, Soft Matter Phys.*, 2011, **84**, 031926.



68 A. Hossein and M. Deserno, *Biophys. J.*, 2020, **118**, 624–642.

69 J. Ehrig, E. P. Petrov and P. Schwille, *New J. Phys.*, 2011, **13**, 045019.

70 B. Camley, C. Esposito, T. Baumgart and F. Brown, *Biophys. J.*, 2010, **99**, L44–L46.

71 B. Camley and F. Brown, *Phys. Rev. Lett.*, 2010, **105**, 148102.

72 K. Kikuchi, M. Yoshida, T. Maekawa and H. Watanabe, *Chem. Phys. Lett.*, 1992, **196**, 57–61.

73 L. C.-L. Lin and F. Brown, *Phys. Rev. Lett.*, 2007, **93**, 256001.

74 E. Reister-Gottfried, S. Leitenberger and U. Seifert, *Phys. Rev. E: Stat., Nonlinear, Soft Matter Phys.*, 2007, **75**, 011908.

75 M. Manghi, X. Schlagberger, Y.-W. Kim and R. Netz, *Soft Matter*, 2006, **2**, 653–668.

76 N. Destainville and N. Coulonges, *Phys. Rev. E*, 2022, **105**, 064115.

77 GROMACS, GROMACS Reference Manual, 2016, <https://manual.gromacs.org/>, Online; accessed June 26, 2020.

78 W. den Otter and S. Shkulipa, *Biophys. J.*, 2007, **93**, 423–433.

79 M. Vögele, J. Köfinger and G. Hummer, *J. Phys. Chem. B*, 2019, **123**, 5099–5106.

80 G. Lindblom and G. Oradd, *Biochim. Biophys. Acta, Biomembr.*, 2009, **1788**, 234–244.

81 S. Aimon, A. Callan-Jones, A. Berthaud, M. Pinot, G. Toombes and P. Bassereau, *Dev. Cell*, 2014, **28**, 212–218.

82 K. Rosholm, N. Leijnse, A. Mantsiou, V. Tkach, S. Pedersen, V. Wirth, L. Oddershede, K. Jensen, K. Martinez, N. Hatzakis, P. Bendix, A. Callan-Jones and D. Stamou, *Nat. Chem. Biol.*, 2014, **13**, 724–729.

83 C. Kluge, M. Pohnl and R. Bockmann, *Biophys. J.*, 2022, **121**, 671–683.

84 H. Noguchi, N. Walani and M. Arroyo, *arXiv*, 2023, preprint, arXiv:2303.09142, DOI: [10.48550/arXiv.2303.09142](https://doi.org/10.48550/arXiv.2303.09142).

85 P. C. T. Souza, R. Alessandri, J. Barnoud, S. Thallmair, I. Faustino, F. Grünewald, I. Patmanidis, H. Abdizadeh, B. M. H. Bruininks, T. A. Wassenaar, P. C. Kroon, J. Melcr, V. Nieto, V. Corradi, H. M. Khan, J. Domański, M. Javanainen, H. Martinez-Seara, N. Reuter, R. B. Best, I. Vattulainen, L. Monticelli, X. Periole, D. P. Tieleman, A. H. D. Vries and S. J. Marrink, *Nat. Methods*, 2021, **18**, 382–388.

86 F. Grünewald, M. H. Punt, E. E. Jefferys, P. A. Vainikka, M. König, V. Virtanen, T. A. Meyer, W. Pezeshkian, A. J. Gormley, M. Karonen, M. S. P. Sansom, P. C. T. Souza and S. J. Marrink, *J. Chem. Theory Comput.*, 2022, **18**, 7555–7569.

87 J. S. Ho and B. A. Straub, *EPL*, 1990, **12**, 395.

88 D. M. Kroll and G. Gompper, *Science*, 1992, **255**, 968.

89 S. Komura, N. Shimokawa and D. Andelman, *Langmuir*, 2006, **22**, 6771.

90 O. H. S. Ollila, H. J. Risselada, M. Louhivuori, E. Lindahl, I. Vattulainen and S. J. Marrink, *Phys. Rev. Lett.*, 2009, **102**, 078101.

91 M. Wieczór, V. Genna, J. Aranda, R. M. Badia, J. L. Gelpí, V. Gapsys, B. L. Groot, E. Lindahl, M. Municoy, A. Hospital and M. Orozco, *Wiley Interdiscip. Rev.: Comput. Mol. Sci.*, 2023, **13**, e1622.

92 C. Chang, V. L. Deringer, K. S. Katti, V. V. Speybroeck and C. M. Wolverton, *Nat. Rev. Mater.*, 2023, **8**, 309–313.

93 C. Gupta, D. Sarkar, D. P. Tieleman and A. Singhary, *Curr. Opin. Struct. Biol.*, 2022, **73**, 102338.

94 L. Casalino, C. Seitz, J. Lederhofer, Y. Tsybovsky, I. A. Wilson, M. Kanekiyo and R. E. Amaro, *ACS Cent. Sci.*, 2022, **8**, 1646–1663.

95 J. V. Vermaas, C. G. Mayne, E. Shinn and E. Tajkhorshid, *J. Chem. Inf. Model.*, 2021, **62**, 602–617.

96 Z. Luthey-Schulten, Z. R. Thornburg and B. R. Gilbert, *Curr. Opin. Struct. Biol.*, 2022, **75**, 102392.

97 J. A. Stevens, F. Grünewald, P. A. M. V. Tilburg, M. König, B. R. Gilbert, T. A. Brier, Z. R. Thornburg, Z. Luthey-Schulten and S. J. Marrink, *Front. Chem.*, 2023, **11**, 1106495.

